Journal of Catalysis 262 (2009) 244–256

Contents lists available at ScienceDirect

Journal of Catalysis

www.elsevier.com/locate/jcat

Local and long range order in promoted iron-based Fischer–Tropsch catalysts: A combined *in situ* X-ray absorption spectroscopy/wide angle X-ray scattering study

Emiel de Smit [a], Andrew M. Beale [a], Sergey Nikitenko [b], Bert M. Weckhuysen [a,*]

[a] *Inorganic Chemistry and Catalysis, Debye Institute for Nanomaterials Science, Utrecht University, Sorbonnelaan 16, 3584 CA Utrecht, The Netherlands*
[b] *Netherlands Organisation for Scientific Research (NWO), DUBBLE @ ESRF, B.P. 220, 38043 Grenoble Cedex 9, France*

ARTICLE INFO

Article history:
Received 24 September 2008
Revised 20 December 2008
Accepted 30 December 2008
Available online 22 January 2009

Keywords:
Fischer–Tropsch synthesis
Iron
Catalyst promotion
In situ
XAFS
WAXS

ABSTRACT

The structural properties of three Fe-based Fischer–Tropsch synthesis (FTS) catalysts containing different amounts of Cu, K and SiO_2 additives were investigated during pretreatment and FTS in a fixed bed-like reactor using combined *in situ* X-ray absorption fine structure (XAFS)/wide angle X-ray scattering (WAXS) techniques. This combination enabled acquisition of complementary information regarding the local environment of iron atoms from XAFS and crystalline phases from WAXS during H_2 and CO/H_2 pretreatment and FTS at 1 bar. The presence of the SiO_2 support and promoter elements significantly influenced the structural properties of the catalysts after pretreatment. After FTS, H_2 pretreated catalysts mainly consisted of amorphous θ-Fe_3C clusters (unsupported catalysts) or amorphous iron (II) silicate (supported catalyst), while the CO/H_2 pretreated catalysts all consisted mainly of γ-Fe and χ-Fe_5C_2. Catalysts activated in CO/H_2 showed superior stability and activity, while H_2 pretreated unsupported catalysts deactivated rapidly during the first 15 h of FTS.

1. Introduction

In Fischer–Tropsch synthesis (FTS), carbon monoxide is catalytically converted through a hydrogenation–polymerization reaction to form hydrocarbon chains [1,2]. FTS enables the production of virtually sulfur and aromatic free transportation fuels and chemical feedstock from carbon sources alternative from crude oil. Depending on the FTS process feedstock and desired products, either cobalt or iron catalysts are applied industrially. Iron-based Fischer–Tropsch catalysts are typically applied for the conversion of synthesis gas from coal [3] and are promising catalysts for the conversion of biomass [4], while cobalt catalysts are mainly used in the conversion of synthesis gas from natural gas [5]. There are several advantages in the use of iron-based catalysts in FTS [6]. However, the main advantage is that iron-based catalysts catalyze the water–gas shift (WGS) reaction. Therefore, these systems can be used in the conversion of syngas with a lower H_2/CO ratio than stoichiometrically needed for the synthesis of long-chain hydrocarbons ($H_2/CO = 2$). As syngas from coal and biomass sources typically have low H_2/CO ratios (1 or less), iron catalysts are especially advantageous for conversion of these syngas types.

Iron-based catalysts typically consist of a precipitated iron oxide phase to which promoters are added to improve catalyst selectivity, activity and stability. The iron oxide catalyst precursors can be activated in H_2, CO or H_2/CO to obtain the active FTS catalyst [7–13]. Typical promoters are Cu, K, and SiO_2. SiO_2 is added to disperse Fe phases and to prevent sintering and attrition of the active catalyst, Cu is added to improve the reducibility of the catalyst and K is used to improve the selectivity of the catalyst toward longer hydrocarbon chains [1,14,15].

Although FTS over iron catalysts was reported as early as the 1920s, the complexity of the iron–carbon–oxide system prevents the straightforward identification of a single active phase and a related reaction mechanism. As a result, there are currently three mechanisms that describe the FTS over iron catalysts that are generally supported in literature [6,16]. As in every catalyst, active sites are located on the surface of the iron catalysts. Nonetheless, the underlying bulk structure may play an important role in determining the nature of these sites and therefore catalytic activity. For this reason, many studies attempt to correlate bulk catalyst composition with FTS performance. It is well established that the iron catalyst consists of a complex mixture of iron carbides (i.e. ε-Fe_2C/ε'-$Fe_{2.2}C$, Fe_7C_3, χ-Fe_5C_2 and θ-Fe_3C), metallic iron (α-Fe) and iron oxide (Fe_3O_4) during FTS. All these phases have been claimed to be active in the synthesis reaction [6].

* Corresponding author. Fax: +31 (0) 30 251 1027.
E-mail address: b.m.weckhuysen@uu.nl (B.M. Weckhuysen).

0021-9517/$ – see front matter
doi:10.1016/j.jcat.2008.12.021

The study of the activated catalysts is challenging in many ways. The complex, dynamic, composition of the catalysts makes straightforward correlation of structure and activity difficult. Moreover, recent work has established that, when not carefully handled, iron catalysts can change composition upon exposure to air [17]. In this respect, the recent development of advanced *in situ* spectroscopic techniques could prove helpful in gaining new insights into the complex system [6,18]. While some authors have carried out their research under (semi) *in situ* conditions [11,19–26], most work relies on the extraction of the catalyst from the reactor bed and subsequent *ex situ* characterization after exposure to air. In addition to this, one of the main characterization methods that is applied to the iron FTS system, X-ray diffraction (XRD), selectively probes crystalline phases. In this respect, XRD is a powerful characterization technique that has been used extensively for the quantification of phases present in the catalyst. However, active iron catalysts often form very small carbide particles under FTS conditions [27]. Since these particles do not show long range ordering, part of the active catalyst may be left undetected in XRD studies. Other techniques that are applied for catalyst characterization, that probe on a more local scale, are often not compatible with *in situ* measurements, either because of the high temperatures involved (e.g. Mössbauer effect spectroscopy (MES)) or because of the gaseous environment (e.g. X-ray photoelectron spectroscopy (XPS)).

Recently, X-ray absorption fine structure spectroscopy (XAFS) was applied to characterize the local order of iron-based FT catalysts [19,28,29]. In XAFS, two spectral regions, the X-ray absorption near edge structure (XANES) and extended X-ray absorption fine structure (EXAFS) provide detailed information about the oxidation and coordination state of the absorber atoms. XAFS is an element selective technique and therefore, selectively probes the surroundings of iron atoms. As XAFS probes the *local* environment of iron species, ill defined, non-crystalline phases that are common in catalysis, are also detected. This can provide important complementary information to other characterization techniques. Finally, XAFS uses a hard X-ray probe (7.112 keV at the Fe K-edge) and therefore can be conveniently applied *in situ*.

In the current contribution we have applied a combined *in situ* X-ray absorption spectroscopy/wide angle X-ray scattering (XAFS/WAXS) setup [30–33] to study catalysts at elevated temperatures (up to ~450 °C) under 1 bar of reactant gas pressure. The measurements were carried out on the samples in a fixed bed-like environment at low conversion. Although industrially FTS is performed at ~20 bar pressure and high (~40%) conversion, our 1 bar, low conversion experiments allowed the systematic study and comparison of three distinct model catalyst systems under differential conditions. Furthermore, the combination of techniques [34] allowed us to study the influence of different pretreatment procedures and FTS reaction conditions on the local *and* long range structure and FTS reaction performance of unpromoted, promoted, unsupported and supported Fischer–Tropsch catalysts.

2. Experimental methods

2.1. Catalyst preparation

Unpromoted Fe_2O_3 (denoted as Fe_2O_3), singly promoted Fe_2O_3/CuO (denoted as Fe_2O_3-Cu) and fully promoted, supported Fe_2O_3/CuO/K_2O/SiO_2 (denoted as Fe_2O_3-Cu-K-Si) iron-based catalyst materials were prepared by precipitation from a ferric nitrate solution in a basic sodium carbonate solution [1]. 25 g of $Fe(NO_3)_3{\cdot}9H_2O$ (Acros, 98+% A.C.S. reagent) was dissolved in 100 mL of distilled water. For the promoted catalysts, 1.2 g of $Cu(NO_3)_2{\cdot}3H_2O$ (Merck, p.a. 99.5%) was added to this solution. The solution was heated to its boiling point, after which it was slowly (~1 min) added to a vigorously stirred, near boiling solution of 25 g Na_2CO_3 in 100 mL distilled water. The resulting precipitate was filtered and re-slurried in about 1 L of near boiling distilled water to remove any residual sodium. This process was repeated about four times, until the pH of the solution was about pH ≈ 7.

For the unpromoted (Fe_2O_3) and singly promoted (Fe_2O_3-Cu) catalyst, the precipitate was dried for ~6 h at 60 °C and subsequently 24 h at 120 °C. The catalyst precursors were calcined in a flow of air at 300 °C for 5 h using a heating ramp of 5 °C/min.

For the fully promoted catalyst (Fe_2O_3-Cu-K-Si), the washed precipitate was re-slurried in 200 mL distilled water. About 8 g of potassium waterglass solution (K_2O:SiO_2 (1:2.15), Akzo-PQ) was added to the slurry under vigorous stirring. 1.5 mL of concentrated HNO_3 was added to precipitate the SiO_2 and lower the total potassium content. After this, the precipitate was dried and calcined in the same way as the unsupported catalysts.

The final catalyst compositions were confirmed by X-ray fluorescence (XRF) analysis on a Goffin Meyvis Spectro X-lab 2000 machine. The relative molar compositions of the catalysts were 100 Fe, 100 Fe/3.9 Cu and 100 Fe/7.5 Cu/5.9 K/15.6 Si for the Fe_2O_3, Fe_2O_3-Cu and Fe_2O_3-Cu-K-Si catalysts, respectively.

2.2. XAFS/WAXS combined setup

The XAFS/WAXS data were collected on the Dutch Belgian Beamline (DUBBLE, BM26A) [33,35] at the European Synchrotron Radiation Facility (ESRF). The storage ring operated at 6 GeV at 50–90 mA in 16 bunch filling mode. A schematic representation of the setup is shown in Fig. 1.

All measurements were performed with the sample mounted in 1.0 mm diameter borosilicate glass capillaries, designed for X-ray applications. The capillary was mounted on a goniometer connected to a gas manifold allowing the supply of He, H_2 and CO gasses [31]. Heating was provided by a calibrated nitrogen heat gun, which allowed treatment temperatures up to 450 °C. The actual temperature of the catalyst bed during treatments was monitored using an external thermocouple.

Fe K-edge (7.112 keV) absorption spectra were collected in transmission mode. The beamline was equipped with a Si(111) double crystal monochromator and a vertically focusing mirror.

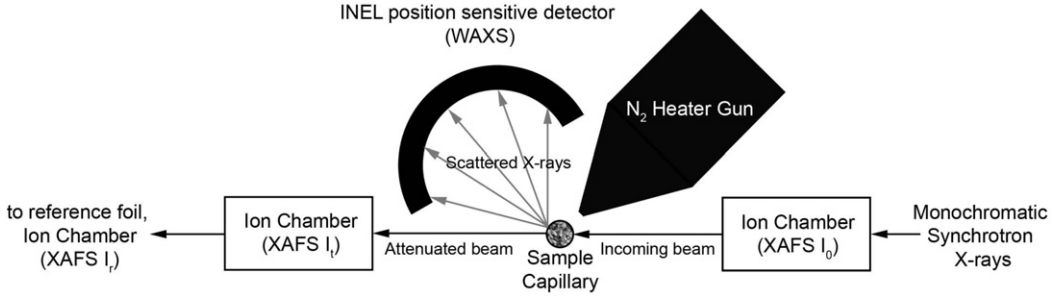

Fig. 1. Schematic drawing of the combined XAFS/WAXS setup at the DUBBLE BM26A beamline at ESRF.

Ionization chambers filled with Ar/He mixtures were used to detect the initial and transmitted signal. The higher harmonics of the primary energy, transmitted by the monochromator, were suppressed with the vertically focusing Si mirror after the monochromator. The factor of suppression for the third harmonic was about ~1000. The overall energy resolution was better than 2.0 eV. A 5 μm reference Fe-foil was measured simultaneously for energy calibration purposes. Average acquisition time for a typical XANES spectrum was ~10 min. EXAFS data were acquired in the quick EXAFS mode, where the monochromator crystal was run at a constant speed in order to reduce the "dead time" of the measurements. Typically, three EXAFS scans were obtained and averaged in order to get better data quality resulting in a total acquisition time of about 45 min.

The WAXS data were collected using a wavelength of 1.781 Å (6.980 keV), well below the Fe K-edge. Scattered (diffracted) light was detected by a position sensitive INEL detector placed above the capillary. The setup allowed a 2θ range of $35° < 2\theta < 80°$. The acquisition time for a diffractogram was typically 10 min.

An online mass spectrometer was used to detect reactants and products in the capillary effluent gas stream.

2.3. Sample preparation

Catalyst samples were diluted with SiO_2 in order to obtain an edge jump of about 1.0–1.5 absorption units in the XAFS data. The use of amorphous SiO_2 ensured that there was no interference between crystalline phases of the diluent and the WAXS signal of the sample. The diluted samples were gently pelletized, ground and sieved to a particle size of 150–250 μm and loaded between plugs of glass wool into the 1.0 mm diameter borosilicate glass capillary. To ensure isothermal heating, the bed length was limited to about 1 cm, about the same size as the "hot spot" of the heater gun. The beam profile was about 500 μm high and 5 mm broad, which ensured that a substantial part of the catalyst bed was probed.

2.4. H_2 activation and in situ Fischer–Tropsch experiments

Samples were activated in H_2 flow (10 mL/min) at 350 °C for 2 h. A heating ramp of 10 °C/min was used. During the ramp and 2 h dwell time, XANES and WAXS data were acquired continuously. After reduction, EXAFS data were collected. For FTS, the sample was cooled down to 250 °C, exposed to a flow of CO and H_2 (4 and 8 mL/min, respectively) and XANES and WAXS data were collected continuously for 4 h. Samples were run under differential conditions. A high gas hourly space velocity (GHSV $\approx 1 \times 10^5$ h^{-1}) further ensured low partial pressures of product H_2O in the catalyst bed during reduction and FTS and therefore low WGS activity. After FTS, EXAFS data were collected from the samples.

2.5. CO/H_2 activation experiments

The activation of the catalyst precursor materials was studied by heating the samples in a mixture of CO and H_2 (4 and 8 mL/min, respectively) to 450 °C at 2 °C/min. XAFS and WAXS data were acquired continuously during the activation treatment. After activation, EXAFS data were collected.

2.6. Catalyst performance testing

Catalytic performance data obtained from the online mass spectrometer was limited due to overlapping hydrocarbon mass fragments. Therefore, separate catalytic performance tests were performed. For this, about 50 mg of sample (particle size 212–500 μm) was diluted in 200 mg SiC to ensure isothermal conditions and loaded into a tubular glass reactor with an internal diameter of 1.0 cm. The reactor was heated using a tubular quartz oven and equipped with thermocouples to monitor the temperature of the catalyst bed. Samples were tested at 1 bar and 250 °C using CO/H_2 (2/4 mL/min) after treatments in either H_2 at 350 °C (5 °C/min) or CO/H_2 at 300 °C/min (2 °C/min) for 2 h. It is noted that though, typically, iron catalysts are tested at much higher pressures (~20 bar), here we chose to use the same pressure as our combined XAFS/WAXS experiment in order to make a fair correlation between the collected characterization data and the catalytic performance. Conversions were kept low (~1%), ensuring differential plug-flow conditions and limiting WGS activity. Product analysis (C_1–C_{20}) was carried out using an online Varian CP-3800 gas chromatograph (GC) equipped with a FID detector and fitted with a 50 m CP-Sil 5 CB column. All reactor lines were kept at 170 °C to prevent the condensation of heavier hydrocarbon products and all products were analyzed from the gas or vapor phase.

2.7. WAXS data analysis

Rough estimations of relative crystal phase contributions after various pretreatments were made by powder diffraction pattern calculation and profile fitting using the Powdercell software package [36].

2.8. XAFS data analysis

EXAFS data reduction was performed using XDAP software [37,38]. The signal-to-noise ratio of the experimental data typically allowed using k ranges of 2.0–10.0 $Å^{-1}$ for the Fourier transform procedure. α-Fe_2O_3, Fe_3O_4, Fe_2SiO_4 and α-Fe references were measured and used as standards for the least squares linear combination fitting of the XANES data and for EXAFS scattering amplitudes and phases. For the phases for which no experimental reference data could be measured; γ-Fe, ε-Fe_2C, χ-Fe_5C_2 and θ-Fe_3C, theoretical scattering phases and amplitudes were calculated using the Artemis program. Least squares linear combination fitting were performed on the normalized XANES spectra and their derivatives using the Athena program. Both programs are part of the IFFEFIT software package [39]. Calculations of scattering phases and amplitudes within this program are performed using the FEFF code [40]. All Fourier transforms presented in this work are k^1 weighted to emphasize contributions from light scatterer atoms (C and O).

3. Results

The reducibility of the Fe_2O_3, Fe_2O_3-Cu and Fe_2O_3-Cu-K-Si catalysts was investigated by heating to 350 °C in H_2 flow while acquiring XAFS and WAXS data. After the H_2 pretreatment, XAFS and WAXS were used to monitor changes in catalyst composition during 4 h of Fischer–Tropsch synthesis at 250 °C in CO/H_2. For comparison, the three catalyst samples were also directly exposed to CO/H_2 flow and heated up to 450 °C, while continuously acquiring XAFS and WAXS data. The H_2 pretreatment and consequent Fischer–Tropsch synthesis will be considered here first.

3.1. H_2 pretreatment: reducibility of the iron catalysts

Clear differences were observed in the reduction behavior of the different catalyst materials under study. Fig. 2 shows the XANES spectra and corresponding WAXS diffractograms of the Fe_2O_3, Fe_2O_3-Cu and Fe_2O_3-Cu-K-Si catalysts during H_2 pretreatment and after different FTS reaction times. At room temperature, the XANES data of all three catalysts show a pre-edge at 7113.5 eV corresponding to the $1s \rightarrow 3d$ electronic transition and a main edge ($1s \rightarrow 4p$) transition at 7123.1 eV, both characteristic for α-Fe_2O_3 [41]. The WAXS data also confirms crystalline α-Fe_2O_3 in

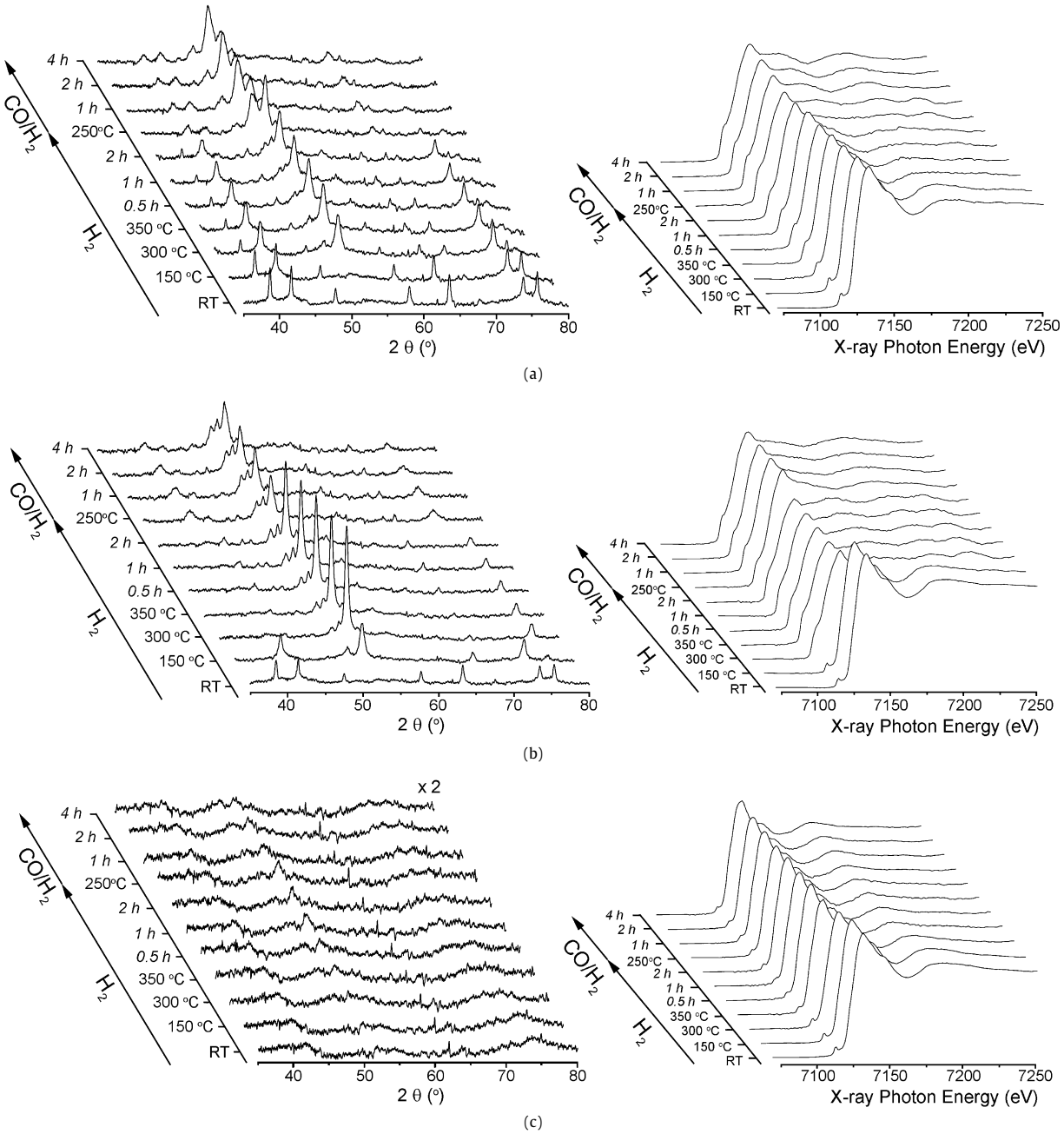

Fig. 2. WAXS diffractograms (left) and XANES spectra (right) of the catalyst materials during reduction in H_2 and Fischer–Tropsch synthesis in CO/H_2. (a) Fe_2O_3, (b) Fe_2O_3-Cu and (c) Fe_2O_3-Cu-K-SiO_2.

the Fe_2O_3 and Fe_2O_3-Cu samples. α-Fe_2O_3 has major contributions at 38.5, 41.4, 57.8, 63.3, 73.6 and 75.5° 2θ originating from the (104), (110), (024), (116), (214) and (300) reflections, respectively. The Fe_2O_3-Cu-K-Si sample does not show a clear contribution of any crystalline phases in WAXS. However, a very broad contribution is observed in the regions typical for α-Fe_2O_3. As the XANES data also suggested the presence of α-Fe_2O_3 in this sample, the catalyst precursor most likely consists of amorphous and/or very small α-Fe_2O_3 crystallites.

Upon exposure to H_2 and heating, the catalysts are slowly reduced. In the XANES data of the Fe_2O_3 catalyst, the edge position gradually shifts from 7123.5 eV toward 7123.0 eV at 350 °C. During the 2 h dwell time at 350 °C, the catalyst is largely reduced to metallic iron, as indicated by the increasing intensity of the edge feature at 7112.0 eV. The XANES spectra and WAXS diffractograms of the three catalysts after 2 h reduction in H_2 at 350 °C are plotted in Fig. 3. Least squares linear combination fitting of the XANES spectrum was carried to the estimate the phase composition of the catalyst material after pretreatment. The reference XANES spectra of α-Fe, Fe_3O_4 and α-Fe_2O_3 were used to fit the experimental spectrum, resulting in a phase composition of 58% Fe^0, 38% Fe_3O_4 and 4% α-Fe_2O_3. The WAXS data for this catalyst show similar trends to the XANES data. The α-Fe_2O_3 phase is initially converted to Fe_3O_4, which has main reflections at 41.5, 67.5 and 74.5° 2θ, originating from the (311), (511) and (440) reflection planes, respectively. Subsequently, Fe_3O_4 is converted to α-Fe, which has two diffractions lines, at 52.1° (110) and at 76.8° (200) 2θ.

As is evident from Fig. 3, there is still a small contribution from α-Fe_2O_3 after 2 h reduction at 350 °C. In addition to the characteristic lines of α-Fe and Fe_3O_4, there is also a small contribution of diffraction lines at 47.6, 50.0 and 50.9° 2θ. These lines are char-

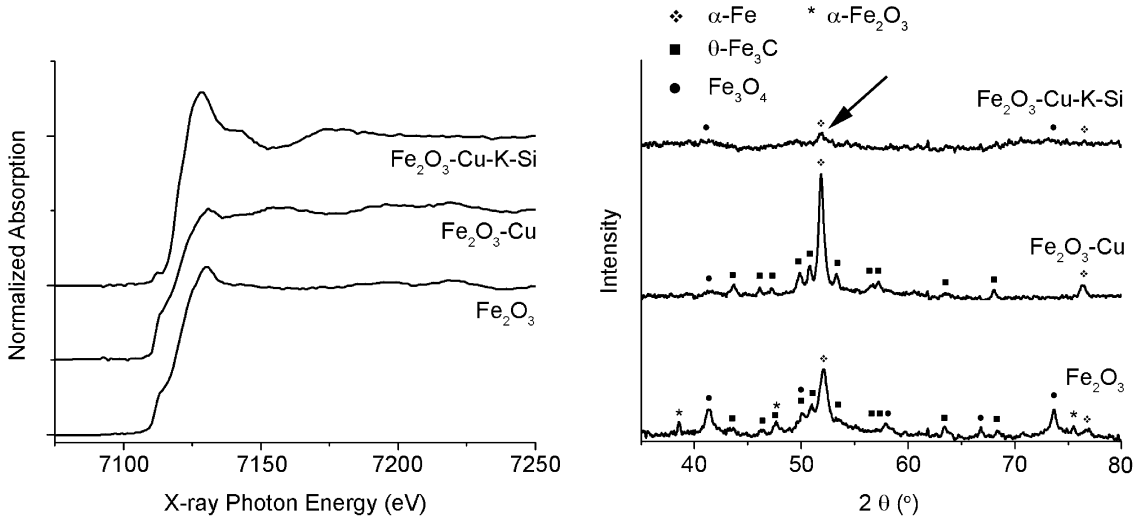

Fig. 3. XANES spectra (left) and WAXS diffractograms (right) of the catalyst materials after treatment in H_2 at 350 °C for 2 h.

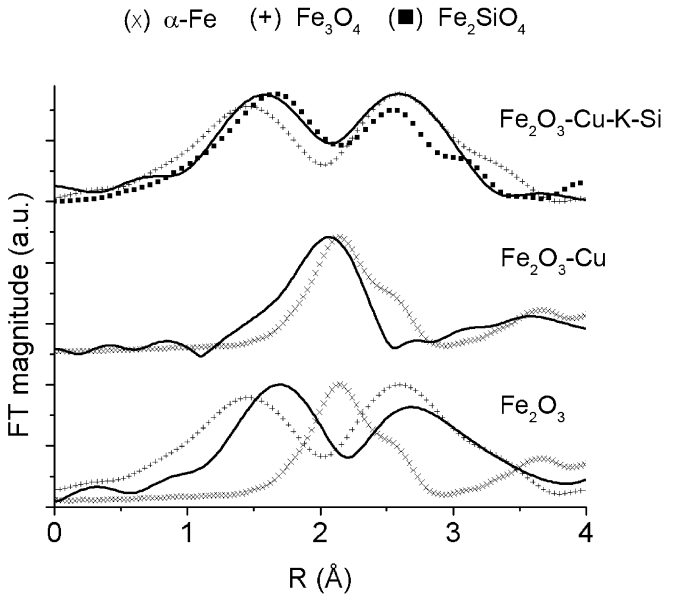

Fig. 4. Fourier transformed EXAFS data of the three catalyst materials after reduction in H_2 at 350 °C for 2 h. The solid line indicates measured data, dotted lines indicate references.

acteristic for the (201), (211) and (102) reflections of θ-Fe_3C [42]. The observation of this phase is rather surprising, as there was no carbon source present in the gas phase. However, it is well known that α-Fe very rapidly dissolves carbon into its crystal lattice after reduction [43]. It is therefore postulated here that, after reduction of the iron oxide to metallic α-Fe, this phase forms from adventitious carbon present on the surface of the catalyst, similar to observations by van der Berg et al. [44].

The non-phase corrected, k^1 weighted, Fourier transformed EXAFS data for the reduced catalyst, represented in Fig. 4, confirms the observations from the WAXS data. The scattering contributions of Fe_3O_4 and α-Fe references show reasonable agreement with the experimental data. The contribution of α-Fe to the Fourier transform is lower than expected from the XANES data. This is most probably due to the k^1 weighting data for the Fourier transform, which increases the weighing of light scatterers (i.e. O and C) relative to heavy scatterers (Fe). The k^3 weighted Fourier transform of the data (not shown here) indeed shows a significantly larger intensity at Fe–Fe scatterer distances characteristic for α-Fe and the relative contribution is closer to the phase composition estimations from XANES.

Fig. 2 illustrates that the Fe_2O_3-Cu catalyst is reduced more rapidly. The XANES data show that at 150 °C, the sample is converted into a mixture of Fe_3O_4 and α-Fe. At 300 °C, it is almost completely reduced to α-Fe. The WAXS data confirm these observations. At 150 °C, all α-Fe_2O_3 has been converted to a mixture of Fe_3O_4 and α-Fe. At 350 °C, the α-Fe is the main crystalline phase. A very broad contribution at 41.5° 2θ indicates the presence of small Fe_3O_4 particles. Again, some θ-Fe_3C is observed after 2 h of reduction. Linear combination fitting of the XANES data yields a phase composition of 84% Fe^0 and 16% Fe_3O_4.

The α-Fe diffraction lines are much sharper in the Fe_2O_3-Cu sample compared to the unpromoted Fe_2O_3 sample. From the broadening of the α-Fe (110) diffraction line at 52.1° 2θ, an estimate of the particle size of both catalysts after reduction was made using the Scherrer equation [45]. The Fe_2O_3 catalyst had an average α-Fe crystallite size of 20.0 nm, while the Fe_2O_3-Cu catalyst had an average crystallite size of 30.6 nm (Table 1).

The Fourier transformed EXAFS data (Fig. 4) for this catalyst confirm that the catalyst is largely reduced after H_2 treatment. There is some Fe-O scattering observed around ~1.4 Å due to the presence of Fe_3O_4.

Overall, XANES, EXAFS and WAXS data clearly indicate that copper promotes the reduction of iron oxide phases to α-Fe.

The fully promoted Fe_2O_3-Cu-K-Si catalyst reduces much slower than the unsupported catalysts (Fig. 2). Even after 2 h of reduction at 350 °C, the XANES spectrum (Fig. 3) shows a strong intensity at ~7125 eV, characteristic for the presence of iron in 2+ or 3+ oxidation state. The edge position after reduction is about 7123.0 eV. Least squares linear combination fitting with α-Fe and Fe_3O_4 does not yield a good fit, suggesting the presence of a third phase. It is well known in literature, that reduction from α-Fe_2O_3 to α-Fe proceeds through Fe_3O_4 and FeO, respectively. FeO is not normally observed in the reduction of unsupported (bulk) catalysts but is often observed in supported catalysts. Strong interaction with the support material (especially in the case of SiO_2) can lead to the formation of iron (II) silicate (Fe_2SiO_4) species [25,46,47]. The XANES spectrum indeed resembles literature spectra [48] and our reference spectrum. The Fourier transformed EXAFS data for this sample, represented in Fig. 4, fits the reference data when the contribution for both Fe_3O_4 and Fe_2SiO_4 are included. Therefore, it is concluded here that a poorly crystalline Fe_2SiO_4 phase forms during reduction of the supported catalyst. Linear combination fitting yields a phase composition of 6% Fe^0, 64% Fe_3O_4 and 30% Fe_2SiO_4.

Table 1
Estimated Fe metal crystallite sizes and detected phases after pretreatment and FTS.

Catalyst	Pretreatment	Metallic phase	Lattice constant (Å)	Metal crystallite size after pretreatment[a] (nm)	Phase composition from XANES after H_2 reduction treatment	Observed phases from WAXS after 4 h FTS[b]	Observed phases from EXAFS after 4 h FTS
Fe_2O_3	H_2	α-Fe	2.87	20.0	58% Fe^0 38% Fe_3O_4 4% α-Fe_2O_3	ε-Fe_2C/ε'-$Fe_{2.2}C$, θ-Fe_3C, Fe_3O_4, χ-Fe_5C_2, α-Fe	θ-Fe_3C, α-Fe
	CO/H_2	γ-Fe γ'-Fe	3.55 3.58	44.6 28.6	–	γ-Fe, χ-Fe_5C_2	γ-Fe, χ-Fe_5C_2
Fe_2O_3-Cu	H_2	α-Fe	2.88	30.6	84% Fe^0 16% Fe_3O_4	θ-Fe_3C, χ-Fe_5C_2, Fe_3O_4, α-Fe	θ-Fe_3C, α-Fe
	CO/H_2	γ-Fe γ'-Fe	3.55 3.58	26.4 29.9	–	γ-Fe, χ-Fe_5C_2	γ-Fe, χ-Fe_5C_2
Fe_2O_3-Cu-K-Si	H_2	α-Fe	–	<10	6% Fe^0 64% Fe_3O_4 30% Fe_2SiO_4	–	Fe_3O_4, Fe_2SiO_4
	CO/H_2	γ-Fe	3.57[c]	12.0[c]	–	γ-Fe, χ-Fe_5C_2	γ-Fe, χ-Fe_5C_2

[a] As calculated from WAXS using Scherrer's equation.
[b] In order of estimated relative abundance.
[c] Data from possibly overlapping peaks.

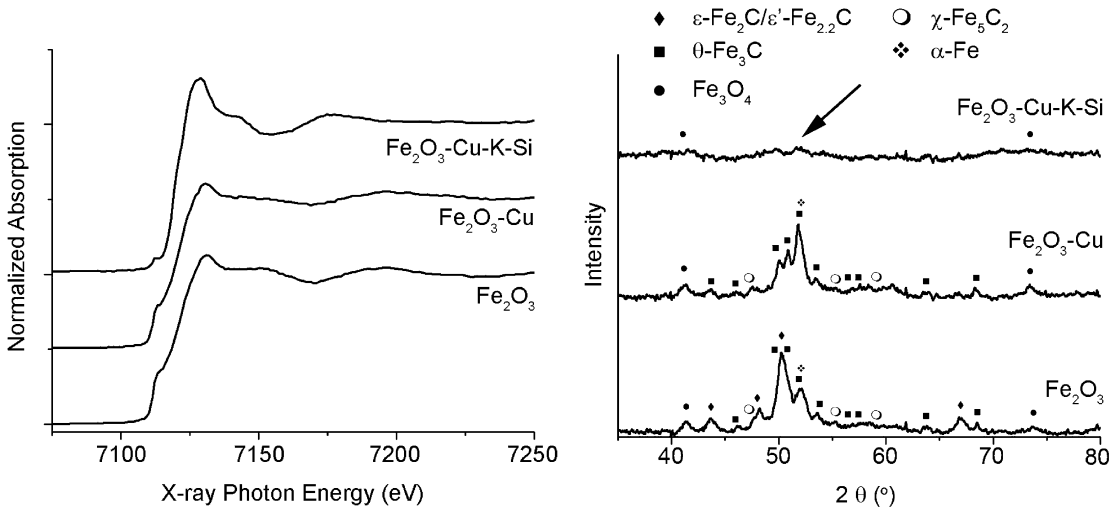

Fig. 5. XANES spectra (left) and WAXS diffractograms (right) of the catalyst materials after treatment in H_2 at 350 °C for 2 h and subsequent Fischer–Tropsch synthesis in CO/H_2 at 250 °C for 4 h.

The WAXS data show a low intensity, broad, α-Fe peak after reduction, indicating a crystallite size of well below 10 nm. There is also a broad contribution from Fe_3O_4 in some regions of the diffractogram, again pointing to very small or poorly crystalline particles. The Fe_2SiO_4 phase, observed from the XAFS data, is not clearly resolved in the WAXS data.

An overview of metal crystallite particle sizes, lattice constants and calculated phase compositions after H_2 pretreatment is presented in Table 1.

3.2. Phase transformations in the H_2 pretreated catalysts during Fischer–Tropsch synthesis

After cooling to 250 °C, FTS was initiated by switching the gas flow to CO/H_2. The XANES spectra and WAXS patterns during FTS are shown in Fig. 2. The same data after 4 h FTS are shown in Fig. 5.

The XANES data of the Fe_2O_3 sample show a significant increase in the feature at 7112.0 eV, indicating further reduction of iron species under FT conditions. Furthermore, a slight shift (0.5 eV) of the edge position to lower energies and an enhanced intensity at ~7130 eV are observed, characteristic for the presence of a carbide phase [28,49–52]. It is noted here that there are few papers dealing with the near edge structure of iron carbide phases and because of the instability these phases, the only carbide phases considered in these papers are the stable θ-Fe_3C [50–52] or a mixed Fe_xC phase [28,49]. As α-Fe and iron carbides generally have quite similar near edge structures, and no reliable iron carbide reference materials were available, we use the b.c.c. α-Fe reference to estimate the total amount of carbides (Fe_xC) present under the assumption that most reduced iron species are present as carbides (evidenced by the WAXS data). Although this assumption might lead to less accurate phase compositions we use this method to give an indication of the amount of carbide species relative to Fe_3O_4.

The least squares linear combination fitting of the XANES data after 4 h of FTS yields a phase composition of 92% Fe_xC and 8% Fe_3O_4.

The WAXS data show that immediately after switching to FTS conditions, new diffraction peaks appear in the WAXS pattern. The diffraction peaks at 43.2, 48.1, 50.0 and 66.8° 2θ values are attributed to the (100), (002), (101) and (102) reflections of (pseudo)hexagonal ε-Fe_2C, respectively [53]. Niemantsverdriet et al. later challenged the assignment of this phase and, on the basis

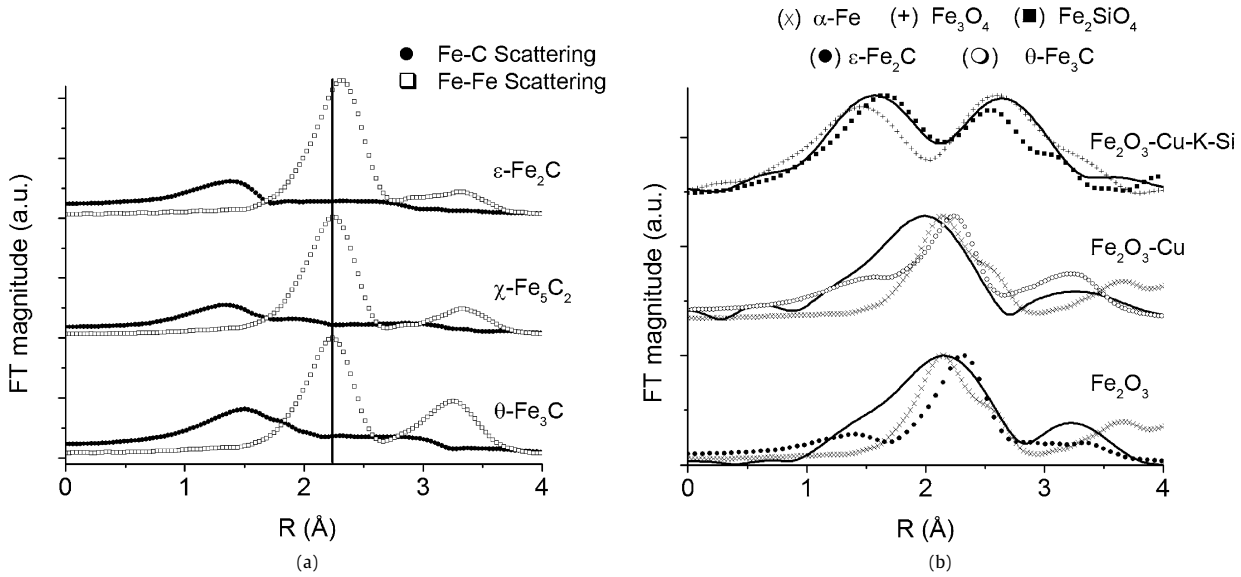

Fig. 6. Fourier transformed EXAFS data of the calculated carbide reference materials (a) and the three catalyst materials after reduction in H_2 at 350 °C for 2 h and subsequent 4 h FTS in CO/H_2 at 250 °C (b).

of Mössbauer experiments, suggested that these peaks were better assigned to the ε'-$Fe_{2.2}C$ phase [54]. This structure is very similar to the former structure, except for a lower overall carbon content and a more disordered crystal structure [55]. A broad diffraction peak is observed at 52.1° 2θ, suggesting that a small part of crystalline α-Fe was might not have been converted to iron carbides after 4 h FTS. However, because of the overlap with the θ-Fe_3C (102) diffraction peak and the very small contribution of the (200) α-Fe diffraction peak, a reliable estimation of the relative amount of α-Fe cannot be made.

The WAXS pattern suggests a smaller contribution of θ-Fe_3C [42] and χ-Fe_5C_2 [56]. A small contribution of Fe_7C_3 [57] could not be ruled out. These carbide phases all show reflections between 49° and 54° 2θ, and peak overlap between these reflections accounts for the broad and unusual peak shape in that 2θ range. The somewhat sharp peaks at 46.3° and 55.3° 2θ can be assigned to the combined (500), (−411) and (020) and the (221) and (2–21) diffraction peaks of χ-Fe_5C_2, respectively. These reflections are distinct for this crystal structure. The broad, underlying contribution in the WAXS pattern at ∼51° and ∼57° 2θ, fits a broadened diffraction pattern of θ-Fe_3C. A rough estimation of relative amount of this phase by theoretical profile fitting of the diffraction pattern shows that, in fact, up to 50 vol% of the sample might consist of θ-Fe_3C. The largest part of the catalyst might thus be present as very small or poorly crystalline θ-Fe_3C carbides.

α-Fe_2O_3, which was present after the reduction step, was consumed during reaction. The α-Fe_2O_3 diffraction peaks disappear from the WAXS pattern after switching to FTS conditions. In addition, it is observed that the (311) reflection at 41.5° 2θ, characteristic for Fe_3O_4, decreases in intensity and broadens somewhat, indicating a decrease in crystallite size.

The EXAFS data analysis confirms the conversion of the Fe_3O_4/α-Fe mixture into a carbide phase. Since not all pure iron carbide reference materials were available, theoretical scattering phases and amplitudes for θ-Fe_3C, χ-Fe_5C_2 and ε-Fe_2C were calculated using the FEFF code [40]. Normalized contributions of iron and carbon scatterers of the different carbide phases are shown in Fig. 6a. The amount of carbon dissolved in the iron lattice increases from θ-Fe_3C > χ-Fe_5C_2 > ε-Fe_2C. However, the relative contribution of the carbon scatterer does not follow this trend as the contribution of the iron scatterer in the different phases changes as well and is highest for the high symmetry ε-Fe_2C carbide. It can be seen that the first iron coordination shell shifts from 2.2 Å in θ-Fe_3C to 2.3 Å in ε-Fe_2C as a result of the expansion of the α-Fe b.c.c. lattice (first shell Fe–Fe 2.1 Å (uncorrected)) to accommodate the higher amount of dissolved carbon.

Fig. 6b shows the EXAFS data of the Fe_2O_3 sample after 4 h FTS, along with the theoretical contributions of α-Fe and ε-Fe_2C. The relatively high intensity of the scattering contribution at 3.2 Å and the high contribution at short scattering distances does not fit the theoretical ε-Fe_2C reference correctly and may suggests a major presence of "carbon lean" θ-Fe_3C instead of the "carbon rich" ε-Fe_2C/ε'-$Fe_{2.2}C$ phase that was observed in WAXS. This supports the earlier estimation that up to 50 vol% of the sample might consist of poorly crystalline or very small θ-Fe_3C particles during FTS.

The Fe_2O_3-Cu sample reacts quite differently under FT conditions. In the XANES data recorded during FTS (Fig. 2), a clear shift of the edge position toward higher energies, a decrease in the edge feature at 7112.0 eV, accompanied by an increase in intensity of the feature at ∼7125 eV is observed after the first 30 min of FTS. These changes indicate that the catalyst is partially reoxidized, even in the reducing CO/H_2 atmosphere. The WAXS pattern (Fig. 5) confirms this. Broad Fe_3O_4 diffraction lines appear in the pattern at 41.5° and 74.5° 2θ, indicating the appearance of small Fe_3O_4 crystallites. The α-Fe (110) reflection line at 52.1° 2θ decreases in intensity, while the (200) line at 76.8° 2θ disappears from the WAXS pattern, showing that the phase is almost completely consumed during FTS. At the same time, a very broad contribution around 51° and 57° 2θ appeared. Distinct peaks at 50.0°, 51.0° and 53.6° 2θ can be assigned to the (211), (102) and (112) reflections of θ-Fe_3C, respectively. The asymmetric peak centered at 51.9° 2θ is attributed to a combination of the (220) and (031) reflections of θ-Fe_3C and a small contribution of α-Fe. The broad contribution underlying the sharper θ-Fe_3C peaks again suggests that poorly crystalline, smaller θ-Fe_3C particles are present in the catalyst. Some evidence of crystalline ε-Fe_2C/ε'-$Fe_{2.2}C$, Fe_7C_3 and χ-Fe_5C_2 is found in the diffraction pattern, suggesting a minor presence of these phases. From linear combination fitting of the XANES data, the composition of the catalyst after 4 h reaction time was 86% Fe_xC, 14% Fe_3O_4.

EXAFS analysis confirms the observation from WAXS that α-Fe formed after reduction is readily converted during FTS. Similar to the Fe_2O_3 catalyst, the EXAFS data show (Fig. 6b) that the catalyst is largely converted into an iron carbide phase. The high contribu-

tion at low scattering distances (~1.3 Å) and the high scattering contribution at 3.2 Å fit the theoretical scattering of θ-Fe_3C quite well. This is in agreement with the WAXS data, where a significant contribution of the θ-Fe_3C phase is observed.

The XANES spectrum of the Fe_2O_3-Cu-K-Si catalyst shows a slight increase in the edge feature at 7112.0 eV upon exposure to CO/H_2, indicative for reduction to Fe^0 species. The WAXS pattern also shows small changes. The broad diffraction peak at 52.1° 2θ, attributed to α-Fe, slowly decreases in intensity during 4 h FTS, most likely because of the formation of small iron carbide clusters. Some weak, broad diffraction signals are observed in the regions typical for carbides (~50° 2θ). It is, however, not possible to assign these broad lines to specific carbide phases. Linear combination fitting of the XANES data results in a phase composition of 4% Fe_xC, 66% Fe_3O_4 and 30% Fe_2SiO_4 after 4 h of FTS. EXAFS (Fig. 6b) does not show significant changes after 4 h of FTS. The main scattering peaks that are observed reflect the calculated composition from the linear combination fitting of the XANES data.

The main detected phases by WAXS and EXAFS and the calculated phase compositions from XANES after 4 h FTS are presented in Table 1.

3.3. Effect of direct CO/H_2 activation on the iron phase composition

Activation of the catalyst materials in a mixture of CO/H_2 yielded very different results from H_2 activation. Overall, the catalyst materials were converted much more facilely and all catalyst materials showed roughly the same composition after treatment. The WAXS and XANES data collected during heating in CO/H_2, is shown in Fig. 7.

For the Fe_2O_3 and Fe_2O_3-Cu samples, most of the iron oxide precursor is consumed at 210 °C. The XANES data suggest a slightly faster reduction of the Fe_2O_3-Cu catalyst. However, the difference is very small compared to the differences observed in the case of H_2 reduction. The WAXS data show that both catalysts are converted from Fe_2O_3 to Fe_3O_4, α-Fe and finally into a mixture of χ-Fe_5C_2 and two distinct phases of (face centered cubic (f.c.c.)) γ-Fe. The intensity of the χ-Fe_5C_2 lines at 46.3° and 55.3° 2θ are low, but resolvable. However, since the theoretical reflection intensities of this phase are much weaker compared to γ-Fe, the amount of this carbide phase in the samples is substantial. The XANES and WAXS data of the three catalysts after CO/H_2 treatment are shown in Fig. 8. From the WAXS data, lattice parameters for both γ-Fe phases were calculated. The lattice parameters were $a\ (=b=c) = 3.55$ Å and 3.58 Å. The occurrence of a second γ-Fe phase (at lower 2θ) above 400 °C, suggests that γ-Fe is partially converted into another, expanded, γ'-Fe phase. This is probably a result of dissolution of more carbon into its f.c.c. crystal structure.

For the Fe_2O_3-Cu-K-Si catalyst, the XANES results show that the catalyst is not completely reduced even after reaching 450 °C (Figs. 7 and 8). Typical reduction steps appear to be delayed by about 50 °C when compared to the Fe_2O_3 and Fe_2O_3-Cu catalyst.

The XANES data of the three catalyst materials could not be fitted correctly by using the α-Fe reference. Therefore, estimated phase compositions are not reported here. It can be seen from the data, however, that the reduction degree of the catalysts compares as Fe_2O_3-Cu-K-Si < $Fe_2O_3 \leqslant Fe_2O_3$-Cu.

Diffraction lines were exceptionally broad in this sample, indicating a very small crystallite size. The intensity of the two diffraction peaks at 450 °C was significantly lower in this sample, indicative for a lower overall crystallinity of the material. The calculated crystallite sizes and unit cell lattice constants for the three different catalysts are reported in Table 1. A small, broad contribution of χ-Fe_5C_2 was observed in the WAXS pattern of this catalyst. A rough estimation of the relative amount of crystalline phases was made by fitting the data. The vol% of χ-Fe_5C_2 changed from 20% in the Fe_2O_3 and Fe_2O_3-Cu-K-Si sample to 30% in the Fe_2O_3-Cu sample.

The Fourier transformed EXAFS data for the three catalysts are plotted in Fig. 9. Similar to the WAXS data, the EXAFS data of the three catalysts do not show major differences. The main scattering contribution at ~2.1 Å fits a combination of the calculated scattering contributions of γ-Fe and χ-Fe_5C_2. There is a clear contribution at 1.3 Å for all three catalysts, which fits the calculated carbon scattering contribution of the carbide phases. This contribution increases from Fe_2O_3 < Fe_2O_3-Cu < Fe_2O_3-Cu-K-Si. This, in combination with the increasing broadness of the main scattering contribution at ~2.1 Å and the scattering contribution at ~3.3 Å from Fe_2O_3 < Fe_2O_3-Cu < Fe_2O_3-Cu-K-Si, suggest that the carbide content of the Fe_2O_3-Cu-K-Si catalyst may be larger than for the two unsupported catalysts, and larger than one would expect on the basis of the WAXS analysis. This is a strong indication that, as was observed for the γ-Fe phase in this sample, the χ-Fe_5C_2 carbide phase is less crystalline and/or smaller than in the other two samples.

Metal crystallite sizes, lattice constants and detected phases from WAXS and EXAFS after CO/H_2 pretreatment are reported in Table 1.

3.4. Catalytic performance

The performance of the activated catalysts for both pretreatments is summarized in Fig. 10 and Table 2. Immediately after activation in H_2, both the Fe_2O_3 and Fe_2O_3-Cu catalyst show FTS activity. Within roughly 3 h, the activity drops to half of its initial value for these catalysts and after 10 h the activity is almost stable, although it slowly continues to decline with time on stream. The C_{5+} (chains of five carbon atoms and longer) selectivity of the Fe_2O_3 catalyst dramatically decreases with time as the CH_4 selectivity increases from 6% to 19%. The Fe_2O_3-Cu catalyst shows a less dramatic decrease in selectivity to longer hydrocarbon chains after 15 h FTS.

The fully promoted Fe_2O_3-Cu-K-Si catalyst shows very different catalytic performance with time on stream. After activation in H_2, the catalyst slowly becomes active, reaching steady state after about 5 h on stream. After 15 h the catalyst is more than twice as active as the Fe_2O_3 and Fe_2O_3-Cu catalysts. However, the C_{5+} selectivity is somewhat lower than for those catalysts, stabilizing at 40% with a CH_4 selectivity of 17%.

The CO/H_2 activated catalysts showed distinct catalytic behavior. When treated in CO/H_2 at 350 °C or 450 °C (not shown here), the catalysts showed almost no FTS activity. Heating slowly (2 °C/min) in a mixture of CO/H_2 up to 300 °C or lower, resulted in very active, selective and stable catalysts. The performance of the catalysts after this treatment is shown in Fig. 10 and Table 2. It can be seen that all three catalysts show initial FTS activity, while the Fe_2O_3-Cu and Fe_2O_3-Cu-K-Si catalysts continue to grow more active within the first 15 h time on stream. The CH_4 and C_{5+} selectivity of the catalysts after 15 h are comparable. The catalytic performance of the Fe_2O_3-Cu catalyst is clearly superior with 68.2% C_{5+} selectivity and a conversion of 3.80×10^{-6} mol CO g Fe^{-1} s^{-1}.

It should be noted here that though the Fe_2O_3-Cu-K-Si catalyst contained K, no typical influence of this promoter on the catalyst selectivity was observed in the catalytic tests. This might be due to the low FTS reaction pressure and conversion, where the alkali promotion effect might be less pronounced [14].

4. Discussion

The three iron-based catalyst materials converted in a significantly different way upon H_2 pretreatment, pretreatment in a CO/H_2 mixture, and during FTS.

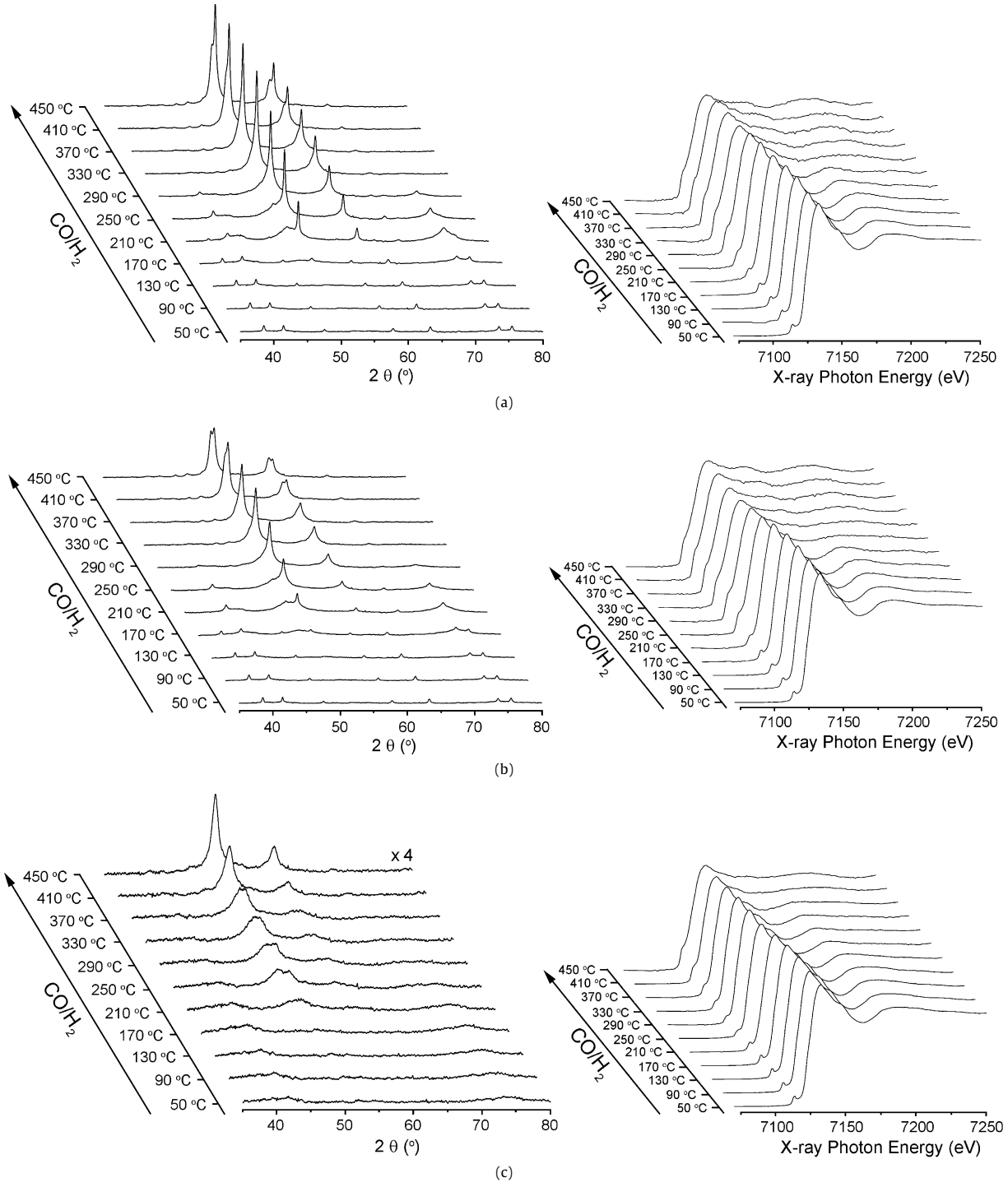

Fig. 7. WAXS diffractograms (left) and XANES spectra (right) of the catalyst materials during treatment in a CO/H_2 mixture at increasing temperatures. (a) Fe_2O_3, (b) Fe_2O_3-Cu and (c) Fe_2O_3-Cu-K-SiO_2.

In the unsupported Fe_2O_3-Cu catalyst, Cu promotes the reduction of the initial iron oxide phase. However, whereas after H_2 treatment the catalyst material is more reduced compared to the Fe_2O_3 catalyst, during FTS it is oxidized and shows similar Fe_3O_4 content. The supported Fe_2O_3-Cu-K-Si catalyst showed very distinct reduction behavior from the two bulk catalysts upon H_2 treatment. Only a very small contribution of metallic α-Fe was observed from WAXS and XANES. The catalyst mainly consisted of Fe_3O_4 and iron (II) silicate (Fe_2SiO_4). The latter phase is likely formed by the strong interaction between Fe^{2+} ($Fe_{1-x}O$) species and the SiO_2 support. Nonetheless, the catalyst showed superior activity and comparable selectivity to the unsupported catalysts after 4 h FTS. It undergoes an induction period and only gradually becomes active. Possibly, the small α-Fe crystallites in this catalyst, in combination with strong interaction with the SiO_2 support causes slower carburization compared to the bulk catalysts and therefore longer activation times. Both the Fe_2O_3 and the Fe_2O_3-Cu catalyst were active from the start of FTS and underwent rapid deactivation.

After CO/H_2 pretreatment, all catalysts show similar composition and consist of γ-Fe along with small χ-Fe_5C_2 crystallites. γ-Fe has not before been reported as a major phase in FTS; only

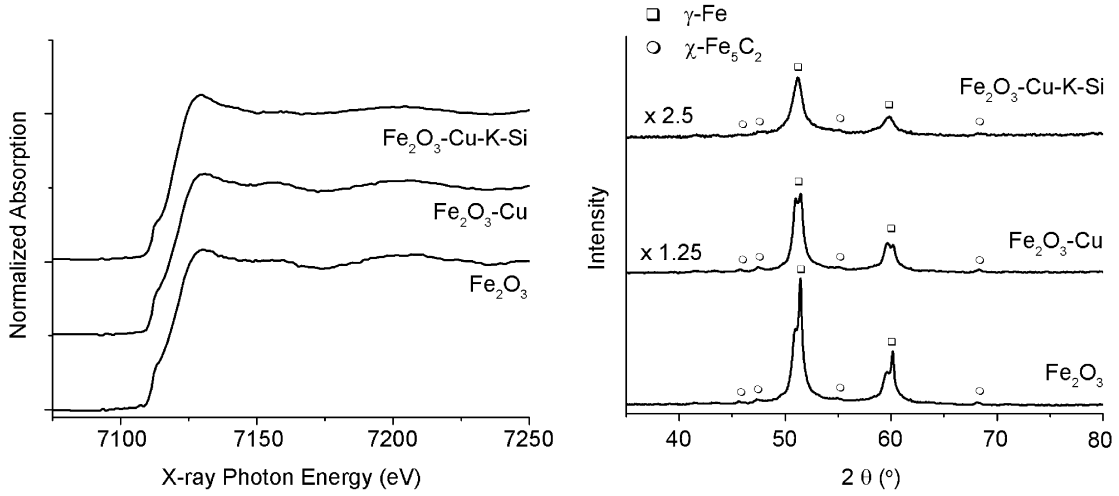

Fig. 8. XANES spectra (left) and WAXS diffractograms (right) of the catalyst materials after treatment in CO/H_2 while heating up to 450 °C with a temperature ramp of 2 °C/min.

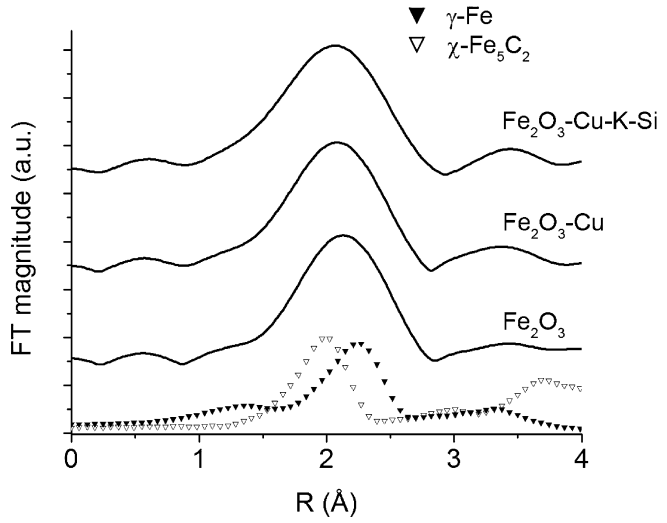

Fig. 9. Fourier transformed EXAFS data of the catalyst materials after treatment in CO/H_2 while heating up to 450 °C with a temperature ramp of 2 °C/min. The solid line indicates experimental data, dotted lines indicate reference compounds.

minor amounts of the phase are sometimes found in spent catalysts. Interestingly, the phase diagram of the Fe–C system indicates that for bulk systems γ-Fe is only formed above 723 °C [58]. This is at significantly higher temperatures than the 250 °C observed for the three catalysts. However, as the catalysts consist of nanometer sized iron oxide particles, the surface enthalpies and energetics of phase transformations might be significantly different from larger crystallites [59]. Furthermore, because our experiments are performed *in situ* in a fixed bed-like reactor, it is possible that γ-Fe is formed under our reactor conditions, but changes through an eutectoid reaction into α-Fe and θ-Fe_3C upon cooling (i.e. the pearlite reaction) [58] and therefore is not typically observed in *ex situ* studies.

Both WAXS and EXAFS show a lower extent of carburization after treatment in CO/H_2 compared to the H_2 treated and subsequently CO/H_2 exposed samples. Apparently γ-Fe is more stable to carburization. It is known that the γ-Fe phase can accommodate up to 2 wt% of carbon before disproportionating to a mixture of iron carbides and γ-Fe. This is significantly more than the 0.02 wt% that α-Fe can dissolve [58]. Therefore, it can be expected that α-Fe is more readily converted to iron carbides and that carbon buildup might proceed faster on α-Fe with respect to the more accommodating γ-Fe structure. This could explain the higher, stable catalytic activity of the CO/H_2 pretreated catalysts after prolonged reaction times.

As expected, the CO/H_2 mixture has more reducing power than H_2. The Fe_2O_3-Cu-K-Si catalyst was largely reduced after CO/H_2 treatment at temperatures as low as 250 °C, while the major part of the iron species remained oxidic in the case of H_2 reduction. Reduction in CO/H_2 also has an important advantage in the sense that no Fe_2SiO_4 is formed during treatment, thereby limiting the loss of iron into the support material and increasing its availability for FTS active species. The fact that no Fe_2SiO_4 is observed suggests an alternative reduction pathway in the case of the CO/H_2 mixture. It is known that above 230 °C at elevated pressure (15 bar), H_2O can react with SiO_2 to form reactive, volatile, $Si(OH)_4$ species [60,61]. In earlier work on supported Fe/SiO_2 catalysts, Dumesic and Lund [62] demonstrated that SiO_2 species can even become mobile at atmospheric H_2O pressure at temperatures around 400 °C. Mobile Si species can react with the partly reduced iron species to form an iron (II) silicate phase. Wielers et al. [46] observed the encapsulation of iron species by iron (II) silicate during H_2 reduction. In their 20 wt% Fe/SiO_2 system, they even suggested that the precursor iron (III) species were completely converted into iron (II) silicates before being reduced to metallic iron at temperatures above 500 °C. A recent *in situ* study performed in our group [25] and our present study strongly confirm these observations. The fact that reduction in CO/H_2 leads to the dominant presence of metallic iron suggest that no mobile, reactive silica species are formed in the presence of CO, possibly due to the reaction of iron oxide species with CO, forming CO_2. Thermodynamically, this is the preferred reaction and mass spectrometry results also show the favored formation of CO_2 over H_2O. The lower resulting H_2O partial pressures may prevent the formation of iron silicates. The CO/H_2 pretreated catalyst showed higher FTS activity and much higher selectivity as compared to the H_2 pretreated catalyst after 15 h on stream. There was no significant difference in reduction behavior between the Fe_2O_3 and Fe_2O_3-Cu sample during the CO/H_2 treatment, in contrast to the H_2 treated catalysts. This further suggests an alternative reduction pathway involving CO. The suggested mechanism for Cu promotion involves the ability of metallic Cu to dissociate hydrogen and consecutive "spill-over" to the iron oxide, thus facilitating reduction. The fact that no clear differences are seen between the samples during CO/H_2 treatment, suggests a limited role of the H_2 reductant and the Cu promotion mechanism.

It is unclear from the data why the catalysts treated at 350 °C and 450 °C in CO/H_2 showed low FTS activity, while those that

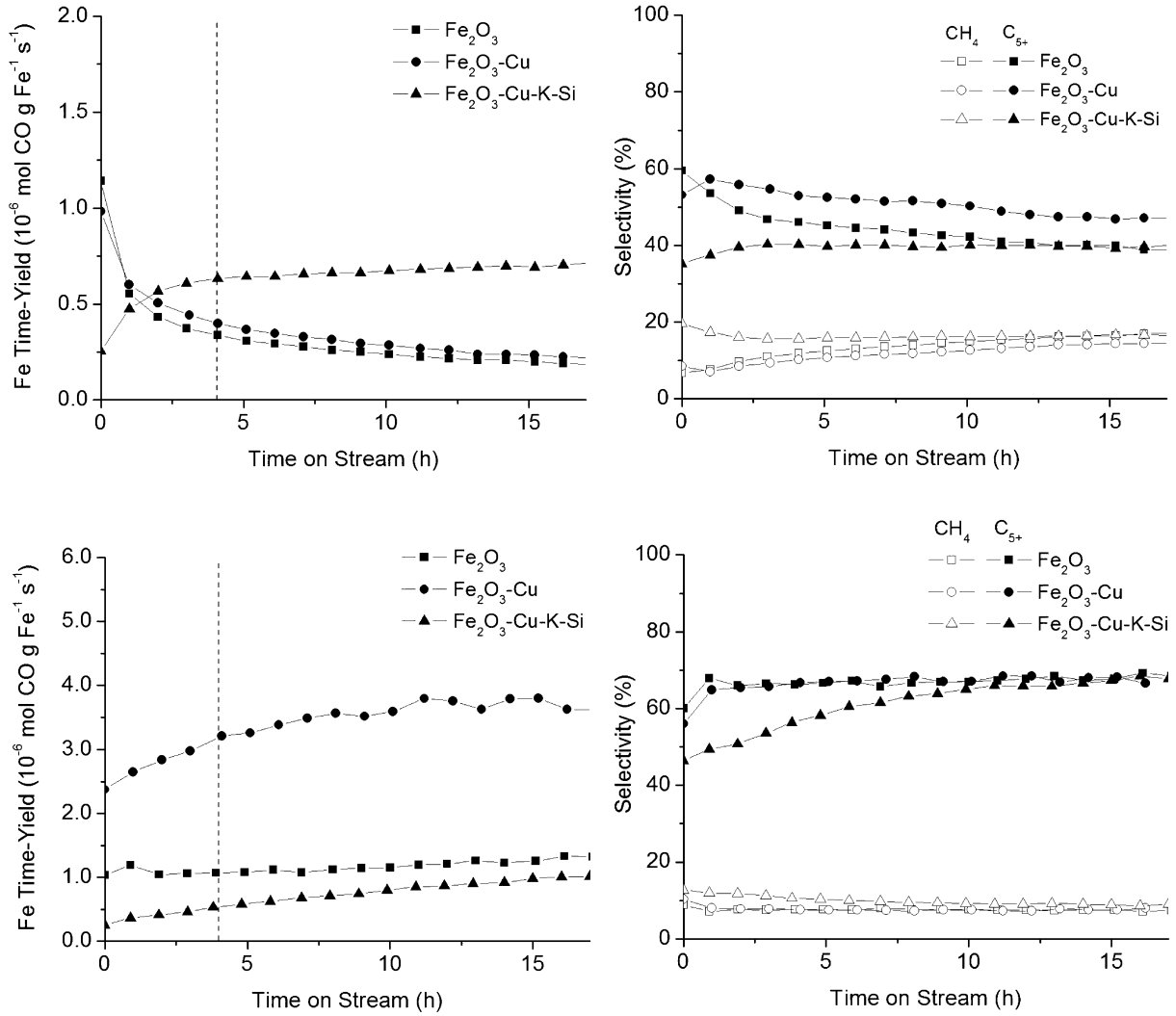

Fig. 10. Fischer–Tropsch synthesis performance data at 1 bar and 250 °C of the three materials after reduction in H_2 at 350 °C for 2 h (upper graphs) and after pretreatment in CO/H_2 while heating up to 300 °C with a heating ramp of 2 °C/min (lower graphs). The dotted line in the graph indicates the end of XAFS/WAXS data collection.

Table 2
Fischer–Tropsch synthesis reaction performance data at 1 bar, $CO:H_2$ (1:2) and 250 °C.

Catalyst	Pretreatment	Activity at $FTS_{t=0\,h}$[a]	Activity at $FTS_{t=4\,h}$[a]	Activity at $FTS_{t=15\,h}$[a]	CH_4 selectivity at $FTS_{t=15\,h}$ (%)	C_{5+} selectivity at $FTS_{t=15\,h}$ (%)
Fe_2O_3	H_2	1.12	0.34	0.20	16.5	39.9
	CO/H_2	1.04	1.07	1.25	7.5	67.7
Fe_2O_3-Cu	H_2	0.91	0.40	0.22	14.4	46.9
	CO/H_2	2.37	3.21	3.80	7.6	68.2
Fe_2O_3-Cu-K-Si	H_2	0.25	0.63	0.69	16.7	39.2
	CO/H_2	0.25	0.46	0.98	8.9	67.3

[a] 10^{-6} mol CO g Fe^{-1} s^{-1}.

were treated below this temperature were very active. Possible explanations might be excessive sintering or the deposition of inactive carbon on the active surface of the catalyst. This was not directly visible in the XAFS/WAXS data. Carbon deposition has been reported in high temperature FTS reaction and is a common cause for catalyst deactivation [54,63,64]. Indeed, Dry et al. reported a tenfold increase in carbon deposition during FTS between 285 °C and 338 °C.

The fact that the H_2 pretreated Fe_2O_3-Cu-K-Si catalyst is more active than the Fe_2O_3 and Fe_2O_3-Cu catalysts after 4 h FTS, even though WAXS and XANES data of the former catalyst indicate only a minor presence of carbide phases, illustrates that it is not straightforward to relate particle sizes and iron phases present in these catalysts to catalyst performance. This study confirms the dynamic nature of iron phases in FTS catalysts during reaction [6]. In view of the activation/deactivation behavior of the catalysts, the number of FTS active sites is expected to change strongly during FTS. The Fe_2O_3-Cu-K-Si catalyst has a higher dispersion than both unsupported systems, but differences in dispersion do not explain the higher activity after 4 h FTS. Interactions with the support material are expected to substantially influence reaction performance of the supported catalyst, as illustrated by the lower degree of reduced species in this catalyst. Furthermore, as noted above, carbon species play an important role in determining the availability of

active surface sites and therefore significantly influence the final performance of the different catalyst systems under study.

A clear correlation between detected crystalline phases and catalyst performance was not always evident. This is not unexpected, as larger crystals, by definition, have a limited surface area on which gas phase reactant can be adsorbed and therefore may play a limited role in determining the catalytic performance of a solid. However, certain crystalline iron carbide phase and/or a particularly active crystal face may still accommodate active surface sites by inducing steric and/or electronic effects, and thereby indirectly influencing the FTS performance. In the case of the CO/H_2 activated catalysts, for example, the amount of crystalline χ-Fe_5C_2 carbides seemed to play a role in the catalyst activity, with the most active catalyst (Fe_2O_3-Cu) showing the largest amount of this carbide phase in WAXS.

The main crystalline phases observed in WAXS were shown to not always be the dominant phases observed from XAFS. In this sense, the local environment of the iron species from EXAFS provided complementary information about the catalyst systems to WAXS. The deactivation of the unsupported H_2 treated catalysts paralleled the occurrence of very small, amorphous θ-Fe_3C clusters, difficult to observe in WAXS. Therefore, based on our results, θ-Fe_3C may play an important role in catalyst deactivation. No θ-Fe_3C was observed in the H_2 reduced Fe_2O_3-Cu-K-Si catalyst and all CO/H_2 pretreated catalyst materials after FTS. Combined with the high relative stability these systems, this suggests that the observed deactivation of the H_2 pretreated, unsupported catalysts might involve the fast formation of a stable (amorphous) θ-Fe_3C phase along with non-stoichiometric amounts of carbon. Unfortunately, we could not directly probe the carbon species deposited on the catalyst materials using our combined setup. However, the formation of θ-Fe_3C is often associated with the buildup of carbonaceous species [65] and it is known that it is difficult to synthesize θ-Fe_3C without some contribution of surface carbon [66,67]. Furthermore, the break-up of θ-Fe_3C crystals into smaller clusters as a result of carbon deposition is commonly reported in literature [68].

It is noted here that in our present study, FTS conditions were limited to differential conditions in order to effectively correlate catalyst structure and performance. Because of this, the extent of catalyst deactivation by oxidation, an important issue in iron-based catalysts [6], was limited. Furthermore, the ambient reactant pressure might have some effect on the bulk iron phases and surface carbon species that are formed during FTS compared to high pressure experiments. Future challenges include studying the system at elevated pressure and high conversion.

5. Conclusion

The characterization of iron-based catalysts in a fixed bed type reactor by *in situ* XAFS/WAXS provided unique insights into local and long range order of iron species during FTS. It was shown that the observations from the two techniques complemented each other. Whereas WAXS showed crystalline phases to be present after activation and during FTS, XAFS analysis suggested that for some catalysts, the majority of iron was present in amorphous phases, which were harder to detect by WAXS.

The two unsupported catalysts were largely reduced after 2 h in H_2 at 350 °C. These materials readily converted to carbides under FTS conditions. Both catalysts deactivated rapidly during the first 4 h of FTS while the SiO_2 supported catalyst was still activating during this time. θ-Fe_3C was the main phase in both unsupported, deactivated catalysts, suggesting an important (indirect) role of this carbide phase in the deposition of carbonaceous species contributing to the overall deactivation process. In the supported iron-based FTS catalyst, almost no crystalline phases were observed during H_2 activation and FTS and the largest part of the catalyst was present as a mixture of Fe_3O_4 and an iron (II) silicate phase, most likely in the form of Fe_2SiO_4. The catalyst activated very slowly during FTS and no crystalline phases were observed, even after 4 h FTS. Activation in CO/H_2 led to the formation of f.c.c. γ-Fe at temperatures above 250 °C in all three catalyst materials. Two distinct γ-Fe phases were observed in the unsupported catalysts after treatment up to 450 °C, possibly owing to the lattice expansion as a result of dissolution of carbon atoms in the γ-Fe f.c.c. structure. A significant contribution (up to 30 vol%) of crystalline χ-Fe_5C_2 was observed in the catalysts. The copper promoter had a less profound effect on the CO/H_2 activation treatment than was the case for H_2 treatment, suggesting an alternative reduction route in the CO/H_2 treatment. This was further confirmed by the absence of iron (II) silicate species in the supported catalyst, suggesting limited mobility of silicon species due to lower partial pressures of H_2O. During FTS, the unsupported catalysts that were activated at 300 °C proved to be more active with time on stream compared to the same catalysts activated in H_2, possibly owing to the prevention of the formation of small θ-Fe_3C clusters and non-stoichiometric amounts of inactive carbon. The activity and selectivity of the three catalysts materials after CO/H_2 activation were superior to the performance of the H_2 reduced catalysts.

The iron-based FTS catalyst system remains a dynamic, complex system and it was shown that the final catalyst structure and performance are strongly dependent on the pretreatment conditions used. Industrially, the FTS reaction pressure and conversion conditions are very different from our present model study. These conditions are expected to play an important role in overall FTS reaction performance and possibly also on the iron phases that are formed. Therefore, future studies will include studying the systems under these conditions.

Acknowledgments

The authors gratefully acknowledge Shell Global Solutions for the funding of this research. Access to the synchrotron facilities at the DUBBLE beamline at ESRF was arranged through the support of the Dutch Science Foundation (NWO) (BM26 DUBBLE-experiment 26-01-788). The beamline staff is kindly acknowledged for their continuous support. Simon Jacques of the University of London, Birkbeck College is kindly acknowledged for providing the capillary goniometer for this experiment.

References

[1] M.E. Dry, in: J.R. Anderson, M. Boudart (Eds.), Catalysis – Science and Technology, vol. 1, Springer-Verlag, New York, 1981, p. 160.
[2] G.P. Van der Laan, A. Beenackers, Catal. Rev.-Sci. Eng. 41 (1999) 255.
[3] B. Wu, L. Tian, L. Bai, Z. Zhang, H. Xiang, Y.W. Li, Catal. Commun. 5 (2004) 253.
[4] E. van Steen, M. Claeys, Chem. Eng. Technol. 31 (2008) 655.
[5] F. Morales, B.M. Weckhuysen, Catalysis, Royal Society of Chemistry, Cambridge, 2006, p. 1.
[6] E. de Smit, B.M. Weckhuysen, Chem. Soc. Rev. 37 (2008) 2758.
[7] T. Herranz, S. Rojas, F.J. Perez-Alonso, M. Ojeda, P. Terreros, J.L.G. Fierro, J. Catal. 243 (2006) 199.
[8] D.B. Bukur, X.S. Lang, J.A. Rossin, W.H. Zimmerman, M.P. Rosynek, E.B. Yeh, C.P. Li, Ind. Eng. Chem. Res. 28 (1989) 1130.
[9] D.B. Bukur, L. Nowicki, R.K. Manne, X.S. Lang, J. Catal. 155 (1995) 366.
[10] A.K. Datye, M.D. Shroff, M.S. Harrington, A.G. Sault, N.B. Jackson, Stud. Surf. Sci. Catal. 107 (1997) 169.
[11] A.J.H.M. Kock, H.M. Fortuin, J.W. Geus, J. Catal. 96 (1985) 261.
[12] A.G. Sault, J. Catal. 140 (1993) 121.
[13] H.H. Storch, N. Golumbic, R.B. Anderson, The Fischer–Tropsch and Related Syntheses, John Wiley & Sons, New York, 1951.
[14] R.A. Dictor, A.T. Bell, J. Catal. 97 (1986) 121.
[15] S. Li, A. Li, S. Krishnamoorthy, E. Iglesia, Catal. Lett. 77 (2001) 197.
[16] B.H. Davis, Fuel Process. Technol. 71 (2001) 157.
[17] M.D. Shroff, A.K. Datye, Catal. Lett. 37 (1996) 101.
[18] B.M. Weckhuysen, Chem. Commun. (2002) 97.
[19] S. Li, W. Ding, G.D. Meitzner, E. Iglesia, J. Phys. Chem. B 106 (2002) 85.
[20] H. Jung, W.J. Thomson, J. Catal. 134 (1992) 654.

[21] L. Guczi, K. Lázár, Catal. Lett. 7 (1990) 53.
[22] M. Pijolat, V. Perrichon, P. Bussière, J. Catal. 107 (1987) 82.
[23] G.B. Raupp, W.N. Delgass, J. Catal. 58 (1979) 361.
[24] J. Xu, C.H. Bartholomew, J. Phys. Chem. B 109 (2005) 2392.
[25] E. de Smit, I. Swart, J.F. Creemer, G.H. Hoveling, M.K. Gilles, T. Tyliszczak, P.J. Kooyman, H.W. Zandbergen, C. Morin, B.M. Weckhuysen, F.M.F. de Groot, Nature 456 (2008) 222.
[26] K. Lazar, Z. Schay, L. Guczi, J. Mol. Catal. 17 (1982) 205.
[27] G. Le Caër, J.M. Dubois, M. Pijolat, V. Perrichon, P. Bussière, J. Phys. Chem. 86 (1982) 4799.
[28] S.Z. Li, R.J. O'Brien, G.D. Meitzner, H. Hamdeh, B.H. Davis, E. Iglesia, Appl. Catal. A 219 (2001) 215.
[29] D. Mahajan, P. Gutlich, J. Ensling, K. Pandya, U. Stumm, P. Vijayaraghavan, Energy Fuels 17 (2003) 1210.
[30] A.M. Beale, A.M.J. van der Eerden, S.D.M. Jacques, O. Leynaud, M.G. O'Brien, F. Meneau, S. Nikitenko, W. Bras, B.M. Weckhuysen, J. Am. Chem. Soc. 128 (2006) 12386.
[31] S.D.M. Jacques, O. Leynaud, D. Strusevich, A.M. Beale, G. Sankar, C.M. Martin, P. Barnes, Angew. Chem. Int. Ed. 45 (2006) 445.
[32] A.M. Beale, L.M. Reilly, G. Sankar, Appl. Catal. A 325 (2007) 290.
[33] S. Nikitenko, A.M. Beale, A.M.J. van der Eerden, S.D.M. Jacques, O. Leynaud, M.G. O'Brien, D. Detollenaer, R. Kaptein, B.M. Weckhuysen, W. Bras, J. Synchrotron Radiat. 15 (2008) 632.
[34] S.J. Tinnemans, J.G. Mesu, K. Kervinen, T. Visser, T.A. Nijhuis, A.M. Beale, D.E. Keller, A.M.J. van der Eerden, B.M. Weckhuysen, Catal. Today 113 (2006) 3.
[35] M. Borsboom, W. Bras, I. Cerjak, D. Detollenaere, D.G. van Loon, P. Goedtkindt, M. Konijnenburg, P. Lassing, Y.K. Levine, B. Munneke, M. Oversluizen, R. van Tol, E. Vlieg, J. Synchrotron Radiat. 5 (1998) 518.
[36] W. Kraus, G. Nolze, Powder cell for powder pattern calculation and profile fitting, version 2.3; available from: http://www.ccp14.ac.uk.
[37] D.C. Koningsberger, B.L. Mojet, G.E. van Dorssen, D.E. Ramaker, Top. Catal. 10 (2000) 143.
[38] M. Vaarkamp, J.C. Linders, D.C. Koningsberger, Physica B 209 (1995) 159.
[39] M. Newville, J. Synchrotron Radiat. 8 (2001) 322.
[40] J.J. Rehr, J. Mustre de Leon, S.I. Zabinsky, R.C. Albers, J. Am. Chem. Soc. 113 (1991) 5135.
[41] M. Wilke, F. Farges, P.E. Petit, G.E. Brown, F. Martin, Am. Mineral. 86 (2001) 714.
[42] D. Fruchart, P. Chaudouet, R. Fruchart, A. Rouault, J.P. Senateur, J. Solid State Chem. 51 (1984) 246.
[43] J.W. Niemantsverdriet, A.M. van der Kraan, J. Catal. 72 (1981) 385.
[44] F.R. van den Berg, M.W.J. Crajé, A.M. van der Kraan, J.W. Geus, Appl. Catal. A 242 (2003) 403.
[45] A.L. Patterson, Phys. Rev. 56 (1939) 978.
[46] A.F.H. Wielers, A.J.H.M. Kock, C.E.C.A. Hop, J.W. Geus, A.M. van Der Kraan, J. Catal. 117 (1989) 1.
[47] C.-H. Zhang, H.-J. Wan, Y. Yang, H.-W. Xiang, Y.-W. Li, Catal. Commun. 7 (2006) 733.
[48] W.E. Jackson, F. Farges, M. Yeager, P.A. Mabrouk, S. Rossano, G.A. Waychunas, E.I. Solomon, J.G.E. Brown, Geochim. Cosmochim. Acta 69 (2005) 4315.
[49] A. Sarkar, G. Jacobs, Y. Ji, H. Hamdeh, B. Davis, Catal. Lett. 121 (2008) 1.
[50] N.S. Kopelev, V. Chechersky, A. Nath, Z.L. Wang, E. Kuzmann, B. Zhang, G.H. Via, Chem. Mater. 7 (1995) 1419.
[51] H. Yamashita, Y. Ohtsuka, S. Yoshida, A. Tomita, Energy Fuels 3 (1989) 686.
[52] S. Takenaka, M. Serizawa, K. Otsuka, J. Catal. 222 (2004) 520.
[53] G.H. Barton, B. Gale, Acta Crystallogr. 17 (1964) 1460.
[54] J.W. Niemantsverdriet, A.M. van der Kraan, W.L. van Dijk, H.S. van der Baan, J. Phys. Chem. 84 (1980) 3363.
[55] H.E. du Plessis, Ph.D. thesis, University of Johannesburg, 2008.
[56] H.E. du Plessis, J.P.R. de Villiers, G.J. Kruger, Z. Kristallogr. 222 (2007) 211.
[57] F.H. Herbstein, J.A. Snyman, Inorg. Chem. 3 (1964) 894.
[58] J. Chipman, Metall. Trans. 3 (1972) 55.
[59] A. Navrotsky, L. Mazeina, J. Majzlan, Science 319 (2008) 1635.
[60] D.H. Everett, J.M. Haynes, P.J. McElroy, Nature 226 (1970) 1033.
[61] M. Prigogine, J.J. Fripiat, Chem. Phys. Lett. 12 (1971) 107.
[62] C.R.F. Lund, J.A. Dumesic, J. Catal. 72 (1981) 21.
[63] M.D. Shroff, D.S. Kalakkad, K.E. Coulter, S.D. Kohler, M.S. Harrington, N.B. Jackson, A.G. Sault, A.K. Datye, J. Catal. 156 (1995) 185.
[64] M.E. Dry, T. Shingles, L.J. Boshoff, C.S. van H. Botha, J. Catal. 17 (1970) 347.
[65] S.A. Eliason, C.H. Bartholomew, Appl. Catal. A 186 (1999) 229.
[66] J.F. Shultz, L.J.E. Hofer, E.M. Cohn, K.C. Stein, R.B. Anderson, Bull. U.S. Bur. Mines 578 (1959) 50.
[67] J.F. Shultz, L.J.E. Hofer, K.C. Stein, R.B. Anderson, Bull. U.S. Bur. Mines 612 (1963).
[68] D.S. Kalakkad, M.D. Shroff, S. Köhler, N. Jackson, A.K. Datye, Appl. Catal. A 133 (1995) 335.